JACS
JOURNAL OF THE AMERICAN CHEMICAL SOCIETY

Article

pubs.acs.org/JACS

Role of Surface Structure on Li-Ion Energy Storage Capacity of Two-Dimensional Transition-Metal Carbides

Yu Xie,*[,†] Michael Naguib,[‡] Vadym N. Mochalin,[‡] Michel W. Barsoum,[‡] Yury Gogotsi,[‡] Xiqian Yu,[⊥] Kyung-Wan Nam,[⊥,#] Xiao-Qing Yang,[⊥] Alexander I. Kolesnikov,[§] and Paul R. C. Kent[†,∥]

[†]Center for Nanophase Materials Sciences, [§]Chemical and Engineering Materials Division, and [∥]Computer Science and Mathematics Division, Oak Ridge National Laboratory, Oak Ridge, Tennessee 37831, United States

[‡]Department of Materials Science and Engineering and A. J. Drexel Nanotechnology Institute, Drexel University, Philadelphia, Pennsylvania 19104, United States

[⊥]Chemistry Department, Brookhaven National Laboratory, Upton, New York 11973, United States

Supporting Information

ABSTRACT: A combination of density functional theory (DFT) calculations and experiments is used to shed light on the relation between surface structure and Li-ion storage capacities of the following functionalized two-dimensional (2D) transition-metal carbides or MXenes: Sc_2C, Ti_2C, Ti_3C_2, V_2C, Cr_2C, and Nb_2C. The Li-ion storage capacities are found to strongly depend on the nature of the surface functional groups, with O groups exhibiting the highest theoretical Li-ion storage capacities. MXene surfaces can be initially covered with OH groups, removable by high-temperature treatment or by reactions in the first lithiation cycle. This was verified by annealing f-Nb_2C and f-Ti_3C_2 at 673 and 773 K in vacuum for 40 h and *in situ* X-ray adsorption spectroscopy (XAS) and Li capacity measurements for the first lithiation/delithiation cycle of f-Ti_3C_2. The high-temperature removal of water and OH was confirmed using X-ray diffraction and inelastic neutron scattering. The voltage profile and X-ray adsorption near edge structure of f-Ti_3C_2 revealed surface reactions in the first lithiation cycle. Moreover, lithiated oxygen terminated MXenes surfaces are able to adsorb additional Li beyond a monolayer, providing a mechanism to substantially increase capacity, as observed mainly in delaminated MXenes and confirmed by DFT calculations and XAS. The calculated Li diffusion barriers are low, indicative of the measured high-rate performance. We predict the not yet synthesized Cr_2C to possess high Li capacity due to the low activation energy of water formation at high temperature, while the not yet synthesized Sc_2C is predicted to potentially display low Li capacity due to higher reaction barriers for OH removal.

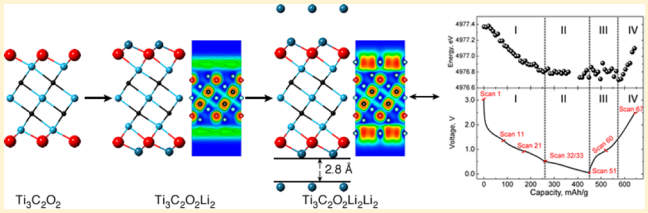

INTRODUCTION

Among portable energy storage technologies, rechargeable Li-ion batteries (LIBs) have attracted the most attention due to their high energy and power densities and reasonable cycle life.[1] Currently, LIBs are widely used in portable electronic devices and regarded as promising power sources for electric vehicles and stationary energy storage applications. The energy and power densities of LIBs are highly dependent on the properties of their electrode materials. The most commonly used anode material is graphite because of its relatively good cyclability and low cost.[2] However, graphite anodes possess a moderate specific Li capacity (theoretical value 372 $mAhg^{-1}$) and suffer from poor rate capability.[2,3] Other potential anode materials, such as transition-metal oxides (TMOs),[4−9] Si, Sn, and Ge-based group IV alloys,[10−12] also face some critical issues including drastic volume changes during Li intercalation/deintercalation, large irreversible capacities, high working potentials, poor electrical conductivities, and low Li diffusivities,[13,14] which currently curtails their wide scale use. Thus, it is necessary to identify new anode materials with enhanced reversible capacities, cycling performances, high-rate capabilities, and safety to meet the requirements for large-scale use.

The flat surfaces and large internal (interlayer) surface areas of layered two-dimensional (2D) materials, such as graphene and MoS_2, potentially allow for high-energy densities and high mobilities.[15] Thus, 2D materials have been viewed as potential anode materials for high-performance LIBs.[16,17] Recently, a new class of 2D early transition-metal carbides and carbonitrides, so-called MXenes, was synthesized by extracting the "A" element from the MAX phases.[18−20] The latter are a large (>60) family of layered, hexagonal ternary early transition-metal carbides, nitrides, and carbonitrides. These solids have a general formula of $M_{n+1}AX_n$ (n = 1, 2, or 3), where "M" is an early transition metal, "A" represents an A group element (mostly group IIIA and IVA), and "X" denotes C and/or N.[21] The extraction was performed by immersing Al-containing MAX powders into hydrofluoric acid (HF) solutions at room temperature (RT).[18,19] This treatment selectively etched away

Received: February 12, 2014
Published: March 28, 2014

   dx.doi.org/10.1021/ja501520b | *J. Am. Chem. Soc.* 2014, 136, 6385−6394

the Al atoms. The surfaces of as-produced exfoliated MXenes—henceforth referred to as functionalized or f-MXenes—are covered by oxygen-containing groups, O and/or OH, and some fluorine, F.[18,22] The f-MXenes usually consist of stacked, multiple functionalized MXene monolayers. The stacks can be further separated to produce delaminated MXenes (d-MXenes) composed of single or a very few (<10) layers[22,23] with overall increased surface area. To date, Ti_2C, V_2C, Nb_2C, Ti_3C_2, Ta_4C_3, $(Ti_{0.5},Nb_{0.5})_2C$, $(V_{0.5},Cr_{0.5})_3C_2$, and Ti_3CN[18,19,24,25] MXenes—all functionalized—have been produced, and it is likely that many more will be synthesized in the near future.

Several studies[18,19,26] have shown that functionalized MXenes are good electrical conductors. Most of these materials are metals with few exceptions,[27,28] e.g., Ti_2CO_2 is a semiconductor with a calculated band gap of 0.88 eV. Moreover, experiments have demonstrated that MXenes are promising anode materials for LIBs.[22,25,29,30] After drying in vacuum, f-Ti_2C, f-V_2C, f-Nb_2C, and f-Ti_3C_2 display Li capacities of 110, 260, 170, and 100 $mAhg^{-1}$ at 1 °C, respectively. The capacity of f-V_2C favorably compares with conventional graphite anodes at similar rates. Note that all else being equal, f-Ti_2C should have the highest gravimetric capacity because it is composed of the lightest atoms. Experimentally, however, f-V_2C has almost triple the gravimetric Li capacity of f-Ti_2C.[25] Along the same lines, f-Nb_2C, which is approximately twice as heavy as f-Ti_2C, also has a significantly higher Li capacity. Intriguingly, the Li capacity of d-Ti_3C_2 (a delaminated MXene with greater surface area) is 410 $mAhg^{-1}$ at 1 C,[22] which is about four times higher than f-Ti_3C_2, and is the highest measured capacity to-date of all MXenes. The latter capacity significantly exceeds the maximum predicted theoretical capacity (320 $mAhg^{-1}$) of Ti_3C_2 monolayers, assuming $Ti_3C_2Li_2$ stoichiometry.[31]

As noted above, all synthesized MXenes are covered with functional groups, which may affect the storage of Li ions. Indeed, at 67 $mAhg^{-1}$,[31] the theoretical capacity of OH terminated Ti_3C_2 monolayers, viz. $Ti_3C_2(OH)_2Li_2$, is only one-sixth of the experimentally measured value for d-Ti_3C_2. The lack of detailed surface structure, the large differences in capacities between exfoliated and delaminated MXenes, and the large discrepancies between theory and experiment all indicate that the actual Li ion storage mechanisms in MXenes may be quite different from those initially proposed.[31]

Here, we performed an extensive investigation of surface structures and Li ion storage capacities of functionalized MXenes. Theoretical simulations and experimental measurements, including X-ray adsorption spectroscopy (XAS) and inelastic neutron scattering (INS) are combined to shed more light on the problem at hand. We first provide a comprehensive picture of the surface structure of MXenes under different conditions. It is then shown that the Li capacity is highly dependent on the surface functional groups. A mechanism that can account for the extra Li capacity of delaminated MXenes is proposed. Lastly, we predict the Li capacities of not yet synthesized f-Sc_2C and f-Cr_2C. Our findings are not only helpful for designing MXene-based anode materials for LIBs but also reveal a possible way to increase the Li capacities for a wide range of 2D materials.

METHODS

Computational Details. First-principles calculations were carried out using density functional theory (DFT) and the all-electron projected augmented wave (PAW) method[32] as implemented in the Vienna ab initio simulation package (VASP).[33] For the exchange–correlation energy, we used the Perdue–Burke–Ernzerhof (PBE) version of the generalized gradient approximation (GGA).[34] Calculations using the van der Waals (vdW) density functional (vdW-DF) of optB86b were performed in some cases.[35,36] Ab initio molecular dynamics (AIMD) simulations were conducted in an NVT canonical ensemble with the Nosé thermostat[37] to investigate the surface structure of MXenes. To determine the energy barriers and minimum energy paths of surface reactions and Li diffusion, we used the climbing image nudged elastic band method (CI-NEB)[38] implemented in VASP. Six to eight images were simulated between initial and final states. More computational details are described in the Supporting Information.

Experiments. To investigate the removal of water from MXenes, f-Nb_2C and f-Ti_3C_2, produced by HF etching of their respective MAX phases at room temperature, were annealed at moderate temperatures in vacuum. To examine the changes in f-Nb_2C and f-Ti_3C_2 due to vacuum annealing, both X-ray diffraction (XRD) and INS were used. *In situ* Ti K-edge XAS spectra were measured for the first lithiation/delithiation cycle of f-Ti_3C_2 to monitor the structural changes during the process. The experimental details for materials synthesis, INS, and XAS experiments are described in the Supporting Information.

RESULTS AND DISCUSSION

Surface Structure after HF Etching. With incomplete or mixed F, O, and/or OH terminations present,[18,20] the surface chemistries of MXenes can be complicated. Although the Li adsorption sites for these terminations have been studied,[27,31] the details of surface structure remain unclear. Therefore, we first examined the surface structure of MXene monolayers after HF etching. We focused on f-Ti_3C_2 because it is, to date, the most studied MXene. Figure 1 shows select AIMD snapshots, as a function of time, of a bare Ti_3C_2 monolayer immersed in 50% (Figure 1a–c), 25% (Figure 1d–f) HF solutions, and water (Figure 1g–i) at 298 K. In all cases, the Ti_3C_2 surfaces

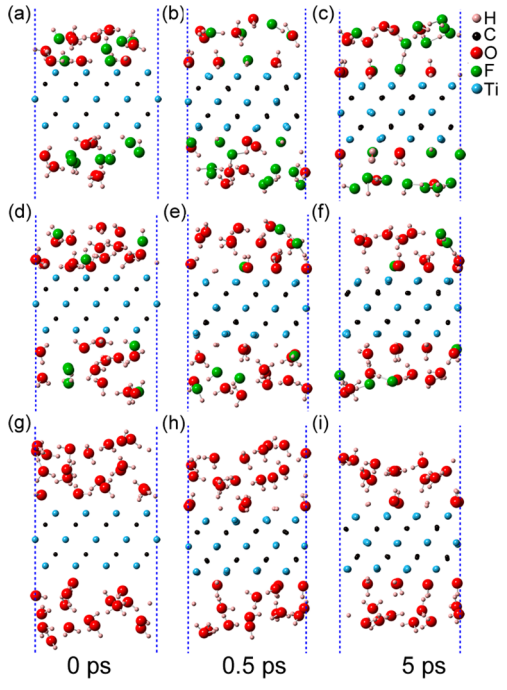

Figure 1. Snapshots at 0, 0.5, and 5 ps of AIMD simulations of a bare Ti_3C_2 monolayer in 50% HF (a–c), 25% HF (d–f), and water (g–i) solutions. Only molecules close to the surfaces are shown. Full configurations are presented in Figure S1. In all cases the surfaces of bare Ti_3C_2 monolayers were rapidly covered with functional groups.

dx.doi.org/10.1021/ja501520b | J. Am. Chem. Soc. 2014, 136, 6385–6394

were rapidly covered with H, F, and OH functional groups. The latter are located on top of the hollow sites between three neighboring C atoms in the layer underneath, which is the same configuration previously predicted by static DFT calculations (labeled configuration I in ref 20). The distances between the functional groups and pointed Ti atoms varied between 3.50−3.65 Å, also in agreement with the static DFT result of 3.64 Å for configuration I-$Ti_3C_2(OH)_2$.[27,31] Moreover, rapid, spontaneous water and HF dissociation were observed in the simulations. Within 0.5 ps (Figure 1b,e,h), the surfaces were already covered with various functional groups. In the 50% HF solution (Figure 1b,c), there is almost the same amount of F and OH terminations. The formation of H_2 molecules was also observed in this solution (Figure 1c, larger H atoms), in agreement with the experimental observation of continued slow gas release during the synthesis, even after all Al has been already reacted with HF, suggesting H is more likely to form H_2 than bind to the surfaces.[18,39] As the concentration of HF decreased (F was consumed by Al in experiments), fewer F groups were formed on the surfaces (compare Figures 1c,f). Noteworthy, and in contradistinction to TiO_2 surfaces, where dissociated and associated water molecules can be coadsorbed, water was fully dissociated on f-Ti_3C_2 surfaces, implying the surface properties of the carbides and corresponding oxides are quite different. The situation for f-Nb_2C was quite similar (see Figure S2.)

Since typically after synthesis, MXenes are washed with water and/or kept in water thereafter, the stabilities of the various functional surface groups in aqueous environments were explored (see Figure S3). From the results (Figure S3a), it is reasonable to assume, within the time scale accessible to our simulations, that the OH groups (Figure S3a) and O groups (Figure S3c) were stable. In contrast, since some F terminations were replaced by O terminations during the simulations (Figure S3b), it would appear that the former are unstable.

When the simulations were repeated by including the vdW interactions, comparable results were obtained (Figure S3d−f). Therefore, we conclude that, after HF etching the MXene surfaces are likely terminated primarily by OH groups, with some F and few O terminations present, in agreement with published X-ray photoelectron spectroscopy (XPS) and energy-dispersive X-ray spectroscopy (EDS) data.[18,22,24,25] Upon washing and/or storing in water, the F surface terminations should gradually be replaced by OH and/or O terminations.

Multilayer Stacking and Water Intercalation. As noted above, the synthesized f-MXenes are multilayered, consisting of a number of MXenes layers separated by surface terminations. To date, the properties of these stacks have not been studied theoretically. Assuming the MXenes surfaces were mostly covered by OH groups, two simplified models, assuming fully OH terminated surfaces, were built: Model A (Figure 2a) was derived directly from the parent MAX phase by simply replacing the Al atoms by OH groups. In this model, OH groups on opposite MXene surfaces face each other, i.e., they sit on a line connecting them (Figure 2a). Model B is the same as model A, but now the *x,y* plane of alternate layers is shifted so that the OH groups terminating one MXene layer nest in the hollow sites between the three nearest OH groups of the facing layer (Figure 2b). Table 1 compares the calculated *c* lattice parameters (*c*-LP) and total energies of f-Ti_2C, f-V_2C, f- Nb_2C, and f-Ti_3C_2 with experimental data. As expected, Model A has consistently larger *c*-LPs. The PBE total energies for model A

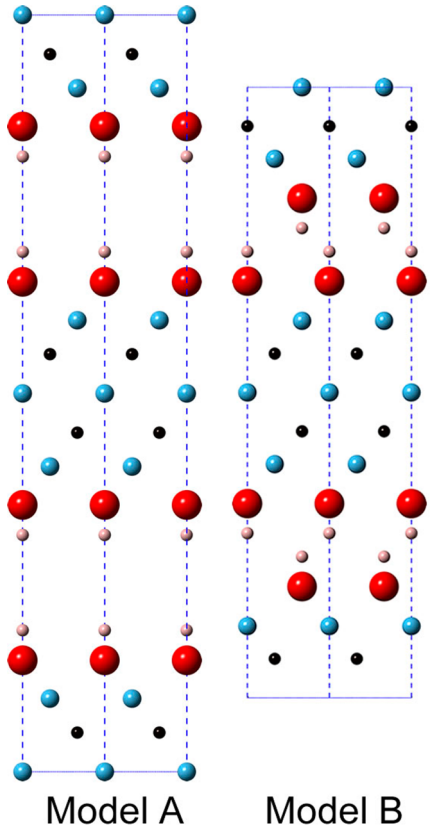

Figure 2. Structural models assumed for DFT calculations of multilayered, i.e., stacked, MXenes.

were lower than model B by 0.1−0.3 eV. However, using the vdW-DF functional, model B became the most stable configuration by 0.1−0.3 eV. The *c*-LPs of model A and B optimized with vdW-DF were also smaller. These results indicate that vdW interactions play an important role in the stacking of MXene layers and contribute to higher stability for model B compared to model A. Note that the computed vdW-DF *c*-LPs for $Ti_2C(OH)_2$ and $Ti_3C_2(OH)_2$ (both in model B) were just ∼1 Å shorter than the experimental results for f-Ti_2C and f-Ti_3C_2 (Table 1). This small difference could be due to temperature effects, imperfect stacking, or a more complicated surface passivation than assumed herein.

However, in contrast to the Ti-based MXenes, the *c*-LPs of f-V_2C and f-Nb_2C were much shorter (5−10 Å) than the experimental results, a fact that was previously attributed to the intercalation of water molecules.[25] To explore this hypothesis, the *c*-LPs of f-V_2C and f-Nb_2C with intercalated water were calculated, and the results (Table 1) show that at least two water layers are required to match the experimental *c*-LPs of unmilled[25] f-V_2C and f-Nb_2C. The average water layer thickness is around 2.3 Å. Compared to unmilled f-V_2C, one additional water layers are needed for milled[25] f-V_2C to match the measured *c*-LP. After water was intercalated, the relative positions of the MXene layers shifted back to model A (Figure S4a,b). It thus appears that the intercalated water molecules weaken the vdW interactions between layers, suggesting that f-MXenes can be separated further into d-MXenes.[22] We also found that the *c*-LPs of MXenes can be expanded to a similar degree as a whole water layer by only a few water molecules (Figure S4c). Therefore, it may not be necessary to form

dx.doi.org/10.1021/ja501520b | J. Am. Chem. Soc. 2014, 136, 6385−6394

Table 1. *c*-LP with or without Water Intercalation and Total Energies[a] of OH Terminated f-MXenes

		PBE		vdW-DF		*c*-LP with intercalated water layers (vdW-DF)		exp.
MXene	model	*c*-LP (Å)	E (eV)	*c*-LP (Å)	E (eV)	2 water layers	3 water layers	*c*-LP (Å)
$Ti_2C(OH)_2$	A	19.474	**−102.18**	18.488	−87.079			15.04[19]
	B	15.068	−102.11	14.769	**−87.255**			
$V_2C(OH)_2$	A	18.474	**−102.55**	17.859	−82.347			23.96,[25,b]
	B	15.247	−102.42	14.431	**−82.419**	19.045	21.287	19.73,[25,c]
$Nb_2C(OH)_2$	A	19.757	**−107.91**	18.631	−88.729			22.34,[25,d]
	B	15.434	−107.62	14.979	**−88.818**	20.965	23.122	
$Ti_3C_2(OH)_2$	A	24.618	**−139.45**	22.995	−119.16			20.51,[19] 20.89,[11] ,[a] 19.99[d]
	B	20.006	−139.36	19.614	**−119.43**			

[a]The total energies of the most stable configurations are in bold face. [b]Milled V_2AlC. [c]Unmilled V_2AlC. [d]Current work.

complete water layers to significantly enlarge the *c*-LPs of MXenes. Imperfections will further change the *c*-LPs.

MXenes after Annealing. In previous studies,[22,25,29] before assembly for electrochemical measurements, the MXene electrodes were dried at 473 K for f-Ti_2C and 413 K for f-V_2C, f-Nb_2C, and f-Ti_3C_2. If there are reactions related to surface OH groups that occur at high temperature, the surface chemistry of MXenes will change. To explore whether the drying temperatures affect the surface structures, the *c*-LP of MXenes with various OH/O ratios were calculated. We found that by simply decreasing the number of surface OH groups, the *c*-LPs of the f-MXenes changed (Figure S5).

Based on the surface structures after HF etching, the following possible high-temperature reactions were considered:

$$M_{n+1}X_n(OH)_2 \rightarrow M_{n+1}X_nO_2 + H_2 \quad (1)$$

$$M_{n+1}X_n(OH)_2 \rightarrow M_{n+1}X_nO + H_2O \quad (2)$$

The calculated reaction pathways and energies for reactions 1 and 2 are shown in Figure S6a,b, respectively. We also used the vdW-DF functional for selected reactions (Figure S7). Since it was found that the energy barriers with, or without, vdW interactions were similar, the focus hereafter will be restricted to PBE energetics and monolayers. The H_2 gas formation reaction (reaction 1) is energetically favorable, but with a high activation barrier (Figure S6a). At 1.57 eV, the Ti-based MXene has the highest activation barrier for this reaction, followed by f-V_2C at 1.35 eV and f-Nb_2C at 1.09 eV. The high activation energy is required to break the two strong OH bonds in reaction 1 (Figure S6d). On the other hand, the calculated energy barrier for water formation (reaction 2) is significantly lower (Figure S6b). This is because in this case only one OH bond needs to be broken (Figure S6g). Some M−O bonds are also broken during the water formation. Here again, the Ti-based MXenes have the highest activation barriers of 1.18 and 1.10 eV for Ti_3C_2 and Ti_2C, respectively. At 0.761 eV, the activation energy for Nb_2C is 0.1 eV higher than that of V_2C (Figure S6b). The energy differences between the final and initial states are also lower in V_2C and Nb_2C (Figure S6b).

To estimate the reaction temperatures, AIMD simulations were carried out. The simulations were performed between 500 and 1500 K in 100 K increments (50 K was used for Ti_3C_2 and Ti_2C when the temperature was higher than 1000 K). Figure S8 shows the high-temperature-induced water formation on OH terminated MXene surfaces. Within the time scale of our simulations, the water elimination onset was found to be approximately 600, 700, 1150, and 1200 K for f-V_2C, f-Nb_2C, f-Ti_3C_2, and f-Ti_2C monolayers, respectively. The onsets of water formation for these MXenes agree well with the NEB energy barriers calculations (Figure S6b), indirectly supporting the validity of the NEB simulations. Increasing the temperature resulted in the formation of more water molecules (Figure S9). At 1500 K some H_2 molecules were formed (Figure S9d), again consistent with the NEB results. It is worth noting here that these simulations were carried out with MXene monolayers; multilayer MXenes may behave differently. For instance, the interlayer spaces of f-Ti_2C and f-Ti_3C_2 are quite small, which may impede water formation (steric hindrance) and/or release (diffusion). On the other hand, these factors should have less influence in f-Nb_2C and f-V_2C due to their larger interlayer distances. Based on these simulations it is reasonable to assume that at a given annealing temperature, the loss of water should be easier for f-Nb_2C and f-V_2C than for f-Ti_2C or f-Ti_3C_2.

To test this idea, f-Nb_2C and f-Ti_3C_2 powders were heated in vacuum at 673 and 773 K, respectively, which resulted in a shift of the (0002) peaks to higher angles in the XRD patterns (Figure 3a,b). These shifts correspond to a *c*-LP decrease from 19.95 to19.37 Å for f-Ti_3C_2 and from 22.34 to15.85 Å for f-Nb_2C. The small *c*-LP change of f-Ti_3C_2 has to be related to a surface reaction since there is no intercalated water to begin with. The large reduction in the *c*-LP for f-Nb_2C, on the other hand, must be mainly due to deintercalation of water molecules from between the layers. To confirm this conclusion, INS measurements for f-Nb_2C were performed. As shown in Figure 3c, the INS spectrum for f-Nb_2C before annealing shows a strong broad peak between 65 and 110 meV that can be assigned to intermolecular librational band of bound water, $\nu_L(H_2O)$, two narrow peaks at 130 and 144 meV that can be related to O−H hydroxyl bending modes, a peak around 205 meV that can be assigned to ν_2 (H−O−H) scissor intramolecular vibration, and another broad peak between 390 and 440 meV that can be explained by a combination of ν_1 and ν_3 s-OH and a-OH water intramolecular stretching modes and stretching modes of O−H hydroxyls. All these peaks indicate the presence of water and hydroxyl groups in f-Nb_2C before annealing. Their disappearance after vacuum annealing (bottom spectra in Figure 3c) confirms their assignment and the concomitant loss of water and OH groups. The strongest band in the spectrum of the vacuum annealed sample, at energies below 30 meV, is probably due to lattice modes involving the heavy Nb atoms; contributions from C atoms are expected to be around 60−80 meV.

In the energy range of intermolecular translational vibrations of bulk water/ice (below 40 meV) in the present data there is only one broad peak at around 20 meV, which is a characteristic feature of strongly *confined* water (for bulk water/ice the INS

dx.doi.org/10.1021/ja501520b | J. Am. Chem. Soc. 2014, 136, 6385−6394

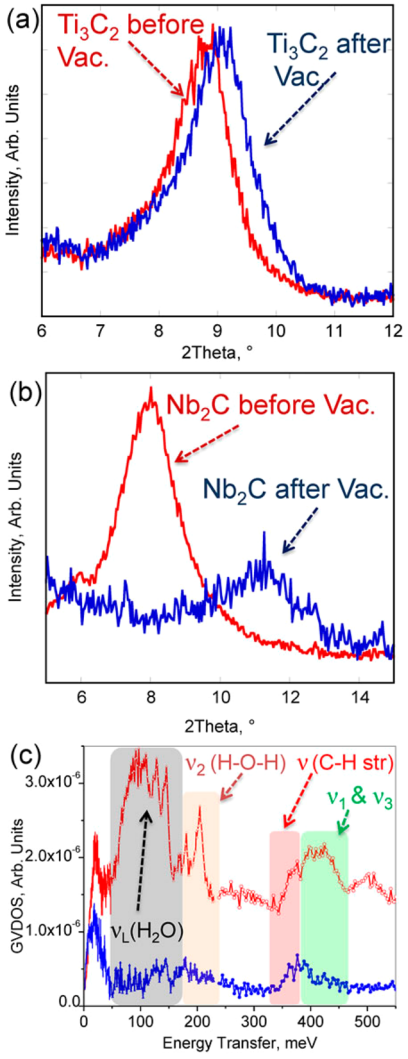

Figure 3. XRD for (a) f-Ti_3C_2 before and after vacuum annealing at 773 K for 40 h (b) Nb_2C sample before and after vacuum annealing at 673 K for 40 h. (c) The generalized vibrational density of states obtained from INS spectra for Nb_2C sample before (red curve) and after (blue curve) annealing.

spectra should exhibit a peak around 6 meV due to transverse acoustic modes of a hydrogen-bonded water network). There are two more peaks in the spectrum before annealing: one around 175 and another around 370 meV. These peaks are also present in the spectra of the sample after the vacuum annealing and can be assigned, respectively, to C−H bending and stretching modes of the ethanol that was used during MXene synthesis and can still be present in the sample in trace amounts (Enyashin et al.[40] have computationally predicted that alkoxy functionalized MXene can form in contact with ethanol, thus the C−H modes could be from a small number of ethoxy functional groups that survived annealing). The origin of these bands is unclear at the moment, inviting further studies. We also measured the weight loss for f-Nb_2C due to annealing, which was ~7%. This is close to the equivalent weight loss due to losing $4H_2$, $2H_2O$ and $4F_{0.3}$ from $4[Nb_2C(OH)_2F_{0.65}]\cdot 2H_2O$ which is ~6.6%. The O and F content before and after vacuum annealing was estimated from EDS (Table S1). Although the number of released water molecules is less than the predictions, it still confirms that the large *c*-LP change of f-Nb_2C after annealing is due to the removal of intercalated water molecules.

When the annealed f-Nb_2C powders were used as an anode in a LIB, no significant change in the performance was observed compared to our previous results in which the f-Nb_2C was dried at 413 K.[25] This suggests that 413 K may be a high enough temperature to drive most of the water and OH groups away from f-Nb_2C or other reactions happen during lithiation.

Li Adsorption and Storage. Due to the complexity of possible surface terminations, herein different fully terminated MXene models were used as extreme cases to address Li storage. Li adsorption on fully OH terminated monolayers was studied first. To assess the stability of Li adsorbed on the MXene surfaces, the adsorption energy was calculated using the expression

$$E_{ad} = (E_{Li-M} - E_M - nE_{Li})/\xi$$

where $E_{Li\text{-}M}$ is the total energy of a lithiated monolayer, E_M denotes the total energy of bare MXene monolayer, E_{Li} is the total energy of bulk bcc Li, and ξ presents the number of adsorbed Li atoms. In this scheme, the lower the E_{ad} value, the stronger the binding of Li to the MXene surfaces. Consistent with previous results for Ti_3C_2,[31] we found that for a 2 × 2 OH terminated monolayer, only two Li atoms—one on either side—could be added (Figure 4a). After Li adsorption, the

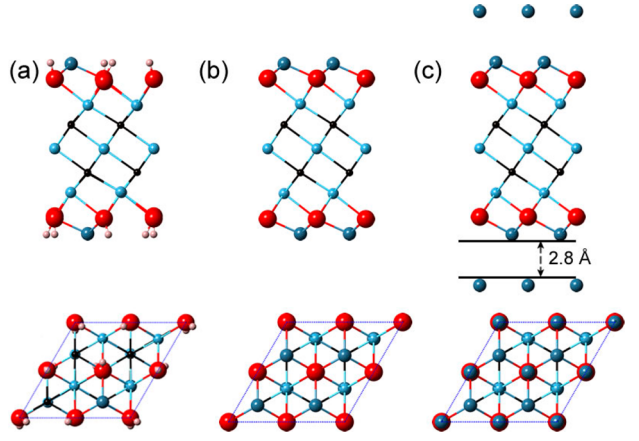

Figure 4. Side and top views of lithiated monolayers of: (a) $Ti_3C_2(OH)_2$ and (b) $Ti_3C_2O_2$; and (c) an extra metallic Li layer adsorbed on top of lithiated viz., $Ti_3C_2O_2Li_2$, monolayers.

nearby H atoms were displaced outward from their original positions (Figure 4a). Using the vdW-DF, E_{ad} was calculated to be 0.124, −0.077, 0.170, and 0.171 eV per Li atom for Ti_2C and V_2C, Nb_2C, and Ti_3C_2, respectively. Therefore, at best, relatively weak Li adsorption occurs on OH terminated MXenes. Our predicted adsorption energy on $Ti_3C_2(OH)_2$ is not in agreement with ref 28, likely due to our use of a self-consistent vdW functional.

The corresponding theoretical Li specific capacities are 95, 91, 58, and 67 $mAhg^{-1}$ for f-Ti_2C and V_2C and Nb_2C and Ti_3C_2, respectively. These capacities are too small, by a factor of up to 4, compared to experimental results.[22,25,29] We also found that it is energetically unfavorable for additional Li atoms to adsorb onto the lithiated, OH passivated, surfaces. Therefore, the OH terminations cannot explain the experimentally measured capacities and, in general, are undesirable for Li intercalation.

dx.doi.org/10.1021/ja501520b | J. Am. Chem. Soc. 2014, 136, 6385−6394

We then focused on O terminated monolayers, where surprisingly, eight—four on either side—Li atoms were directly adsorbed on a 2 × 2 O terminated MXene monolayer (Figure 4b), a number as high as that for bare MXene surfaces.[31] The vertical distance from the adsorbed Li layer to the nearest O is 0.86 Å. The calculated vdW-DF E_{ad} and corresponding theoretical Li specific capacities are listed in Table 2. At −1 to −1.5 eV per Li atom, the O terminated MXenes have lower adsorption energies than bare MXene surfaces,[31] indicating a strong interaction between O and Li. Due to the adsorption of more Li atoms, the Li capacities are almost quadrupled compared to the OH terminated MXenes. By comparing the experimental and theoretical capacities of f-MXenes, we found that while the correspondence between these values is high for f-V_2C and f-Nb_2C, the agreement for Ti_2C is not as good, although theory predicts it to have the highest capacity. This capacity difference may relate to the number of Li atoms adsorbed on the MXene surfaces. Since both O terminated and bare MXenes can hold more Li atoms than OH terminated ones, Li capacity will be maximized by minimizing the number of surface OH functional groups. Reactions between Li and surface OH, resulting in conversion of OH- into O-terminated and/or with partial bare MXenes, are

Table 2. vdW-DF Adsorption Energies (E_{ad}) and Theoretical Li Capacities of O Terminated f-MXenes in Comparison with Experimental Li Capacities

		Li capacity ($mAhg^{-1}$)	
MXene	E_{ad} (eV per Li atom)	theo.	expt.
$Ti_2CO_2Li_2$	−1.364	383	110[29]
$V_2CO_2Li_2$	−1.539	367	260[25]
$Nb_2CO_2Li_2$	−1.019	233	170[25]
$Ti_3C_2O_2Li_2$	−1.404	268	100[22]

$$M_{n+1}X_n(OH)_2 + 2Li \rightarrow M_{n+1}X_nO_2Li_2 + H_2 \quad (3)$$

$$M_{n+1}X_n(OH)_2 + 2Li \rightarrow M_{n+1}X_nOLi_2 + H_2O \quad (4)$$

The calculated reaction energy pathways for reactions 3 and 4 are shown in Figure S10a,b, respectively. The transition state for H_2 formation is similar to that during annealing (Figure S10d). However, in this case the transition state for reaction 4 does not involve the breaking of bond between H and O (Figure S10g), instead every other OH group is eliminated from the surface. This reaction also involves the breaking of M−O bonds.

In contrast to the reactions 1 and 2 at high temperatures, the activation energy of H_2 formation in reaction 3 is slightly lower than that of water formation in reaction 4. The activation energies are 0.503, 0.501, 0.193, and 0.476 eV for OH terminated Ti_2C, V_2C, Nb_2C, and Ti_3C_2, respectively. These values are significantly lower than the activation energies of reactions 1 and 2 and could be achieved experimentally.

From Bader analysis, the adsorbed Li transfers 0.8 *e* to the surrounding O atoms, suggesting a strong bonding between Li and O. Meanwhile, the nearest H atoms gained 0.1 *e* per atom, implying a weakening of the OH bond. On the other hand, the newly formed Li−O bond prohibited O from desorbing from the surfaces. Thus, reaction 4 had a higher energy barrier than reaction 3.

Since most of the OH groups were driven away under high temperature for Nb_2C and V_2C, reactions 3 and 4 should be more pronounced in Ti_2C and Ti_3C_2, where the number of remaining OH groups should still be high. We therefore performed *in situ* XAS on f-Ti_3C_2 during the first lithiation and delithiation cycles (Figure 5), as an example, to experimentally test our proposed reactions and Li storage mechanism. The Ti K-edge XANES spectra feature a relatively weak pre-edge peak, A, at ∼4971 eV, and a strong main absorption peak, B, at around 4986 eV. Similarly to TMOs, the interactions in transition-metal carbides involve the hybridization of the metal 3d and carbon 2p orbitals. The strong p−d hybridization in titanium carbides is confirmed both from band structure calculations and from experimental measurements.[41] Therefore, the first two peaks in the pre-edge, feature A, can be assigned to the transitions of ls electrons to the hybridized orbitals of t_{2g} (Ti 3d + C 2p) and e_g (Ti 3d + C 2p), respectively, while the main absorption peak B is due to the dipole allowed transition of 1s electrons to unoccupied Ti 4p states.

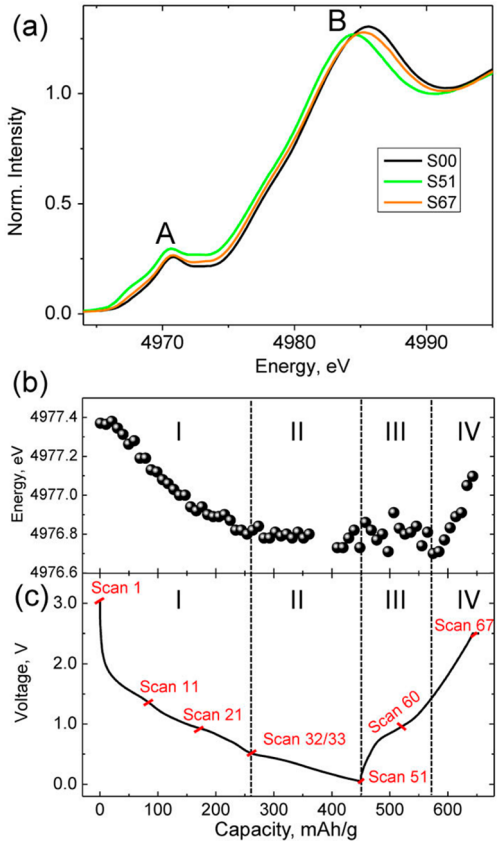

Figure 5. (a) *In situ* Ti K-edge XANES analysis during lithiation and delithiation of f-Ti_3C_2, S00 is XANES before any electrochemical reactions, S51 and S67 refer, respectively, to the fully lithiated and fully delithiated states shown in (c). (b) Variation of Ti edge energy (at half height of normalized XANES spectra) vs capacity during lithiation and delithiation combined with, (c) the corresponding voltage profiles.

The XANES for the Ti K-edge after lithiation (Figure 5b) showed a shift to lower energy indicating a decrease in the average Ti oxidation state. Similar small shifts in the XANES energy and a reduction in the average Ti valence were reported for amorphous titania upon the incorporation of 2.4 Li per TiO_2.[42] For nanocrystalline anatase, the shift is larger and equivalent to a reduction from 4+ to 3+ due to incorporating one Li in per TiO_2.[43] After delithiation, the XANES spectrum shifted back to higher energies (higher Ti oxidation states), but

dx.doi.org/10.1021/ja501520b | J. Am. Chem. Soc. 2014, 136, 6385−6394

not to the initial state. This change during lithiation and delithiation is clear evidence for redox reactions. In agreement with *in situ* XRD results during lithiation for a closely related MXene, f-Ti_2C,[29] there was no evidence for any Ti-conversion reactions.

The variation of the Ti edge energy during lithiation (Figure 5b) showed two distinct regions: region I (>0.5 V), where a continuous decrease in edge energy was observed, followed by region II (<0.51 V), where the energy does not change with further lithiation. Similarly, during delithiation, region III showed a constant edge energy that did not change significantly with increasing voltage, followed by region IV, where the energy increased continuously with increasing voltage. It is important to note that region I ends at a voltage of 0.51 V with a capacity of 262 $mAhg^{-1}$ (Figure 5c). This capacity corresponds to 1.95 Li, i.e., close to 2 Li, per $Ti_3C_2O_2Li_2$ which implies that at that juncture, almost all the OH groups were eliminated during the first lithiation cycle. This is again in agreement with our theoretical predictions. Moreover, the Li capacity of f-Ti_3C_2 reaches 449 $mAhg^{-1}$ at the end of region II, which requires 1.4 extra Li per $Ti_3C_2O_2$. Since the oxidation state of Ti is barely changed in region II (flat Ti edge energy), it is reasonable to assume that the extra Li atoms do not *directly* interact with the Ti layers and may thus be stored on top of $Ti_3C_2O_2Li_2$.

Upon delithiation, the reversible Li capacity of Ti_3C_2 is only 200 $mAhg^{-1}$. These capacity measurements were performed using cyclic carbonate electrolytes, which can be an additional source of capacity loss due to the formation of a solid electrolyte interphase (SEI). The reduction in reversible capacity might therefore also be due to slower Li diffusion due to reaction products, such as H_2O, SEI etc. trapped in the interlayer spaces, or at the edges. Previous XRD studies of f-Ti_2C[30] show an irreversible increase in the *c*-LP on lithiation, implying that there indeed are ions and/or molecules trapped between the MXene layers. Nevertheless, we expect fewer reactions related to OH groups in f-Nb_2C and f-V_2C as the OH concentrations on their surfaces are lower compared to Ti-based MXenes. This is probably one reason why, experimentally, f-Nb_2C and f-V_2C have higher reversible Li capacities as compared to the Ti-containing ones.

The multilayer Li adsorption behavior implied herein for MXenes from the XANES studies above is quite similar to recent reports on graphene.[44,45] Hence, we looked at the extra Li layers adsorption on MXene surfaces (Figure 4c). Since the extra Li layers are actually adsorbed on already lithiated MXenes, the equation to calculate the adsorption energy, E_{ad}, of extra Li layers on MXenes can be recast to read:

$$E_{ad} = (E_{Li-Li-M} - E_{Li-M} - \xi E_{Li\_iso})/\xi$$

In other words, the reference system changes to the total energies of lithiated MXene monolayers and isolated Li atoms. This was done in order to allow for comparison of our results with E_{ad} on graphene. Our calculated vdW-DF bcc Li cohesive energy is −1.645 eV/atom, in good agreement with the experimental result of −1.630 eV/atom.[46] The E_{ad} for the extra Li layer (i.e., 2 extra Li per MXene unit) on Ti_2COLi_2, V_2COLi_2, Nb_2COLi_2, and $Ti_3C_2OLi_2$ is −1.552, −1.541, −1.592, and −1.554 eV per Li atom, respectively. Despite the fact that E_{ad} for the first Li layer differs, not surprisingly, E_{ad} of the extra Li layers is almost the same for all MXenes. Also not surprisingly, these E_{ad} values are comparable to those on graphene (−0.934 to −1.598 eV/atom)[47,48] and are just slightly higher than the bulk Li cohesive energy, suggesting that Li is able to form several layers on top of the already lithiated MXene surfaces.[49]

We also examined the electronic properties of $Ti_3C_2O_2Li_2$ with an extra Li layer. Figure 6 shows the valence electron

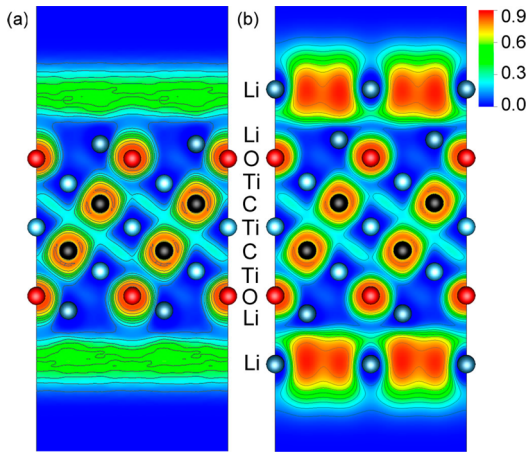

Figure 6. Valence ELF of (110) sections of: (a) lithiated $Ti_3C_2O_2Li_2$ monolayer and (b) with an extra Li layer.

localization function (ELF) of $Ti_3C_2O_2Li_2$ with or without an extra Li layer. From ELF, we can clearly see the electron transfer between C and Ti and between Li and O. Without the extra Li layer, there are few electrons localized above the adsorbed Li layer. With the extra Li layer, the interaction between the different Li layers is clearly visible in the ELF, indicating that the extra Li layer is able to bind to the already lithiated MXene. Moreover, there are no changes in the electrons around the Ti atoms with the extra Li layer. Therefore, the adsorption of the latter on $Ti_3C_2O_2Li_2$ should not noticeably change the Ti oxidation states, in agreement with our XANES results.

By examining how E_{ad} changes as a function of the number of additional Li layers (Figure S11), we found that two more extra Li layers may be formed before a bulk-like arrangement of Li atoms becomes more favorable (the adsorption energies are equal to the Li cohesive energy after a third extra Li layer is added). Thus, the Li capacity could potentially be tripled. This is different from what has been calculated in pristine graphene,[44,45] where after an extra Li layer is attached, E_{ad} falls rapidly to the bulk Li cohesive energy. In the MXenes, the first extra Li layer forms about 2.8 Å above the lithiated surfaces (Figure 4c), which is longer than the distance between the Li atomic layers and graphene sheets ∼2.1 Å.[50] The second and third extra Li layers require 2.3 Å for each layer. Therefore, a large space is needed to accommodate them. Since the reaction products likely prevent or hamper Li intercalation into the interlayer spaces, the extra Li layers are most likely to form at the outmost surfaces and/or edges of the MXene flakes, favoring high surface area samples. Although it was not possible to perform XAS measurements for d-MXenes due to the small thicknesses of samples available to us, the results for f-MXenes can still shed some light on d-MXenes, as the latter can be viewed as f-MXenes with fewer MXene layers. In particular, d-Ti_3C_2 had a significantly larger surface area (∼100 m^2/g) than that of f-Ti_3C_2 (∼20 m^2/g).[23] The corresponding Li capacity of d-Ti_3C_2 is 410 $mAhg^{-1}$, which is 4 times higher than that of f-Ti_3C_2 (100 $mAhg^{-1}$) and requires at least 3 Li per Ti_3C_2 unit.

dx.doi.org/10.1021/ja501520b | J. Am. Chem. Soc. 2014, 136, 6385−6394

Since Ti_3C_2 can only adsorb 2 Li at most as a single layer, the much higher Li capacity of d-Ti_3C_2 is possibly due to the formation of additional Li layers on the larger surface area. These extra layers formed on the outermost layers can at least partially explain why the d-MXenes have higher Li capacities than their stacked counterparts.

Clearly additional studies are required to confirm the mechanism for additional capacity, but our XANES data suggest a distinct adsorption for additional Li layers consistent with our proposed mechanism.

We also estimated the open circuit voltage (OCV) for the following reaction:

$$M_{n+1}X_nO_2 + 2Li \leftrightarrow M_{n+1}X_nO_2Li_2 \quad (5)$$

The average anode OCV between charged (lithiated MXenes) and discharged states is given by $V = -(\Delta G/\xi ZF)$,[51] where F is the Faraday's constant, ξ is the number of intercalated Li atoms, and ΔG is the Gibbs free energy change of reaction 5. Since the volume and entropy changes are negligible in this solid-state reaction, the free energy ($\Delta G = \Delta E + P\Delta V - T\Delta S$) can be approximated by the internal energy change ΔE. With this assumption, the calculated OCVs are 1.539 V for V_2CO_2, 1.019 V for Nb_2CO_2, 1.364 V for Ti_2CO_2, and 1.404 V for $Ti_3C_2O_2$ with respect to pure Li. This trend is in good agreement with experimental results, where f-Nb_2C has the lowest voltages (below 1 V) and f-V_2C has the highest (above 1.5 V), with the Ti-containing phases in between.[25] Noteworthily, the calculated OCVs of bare, OH, or F-terminated MXenes[31] are significantly lower than those of the O terminated MXene studied here and lower than the experimental data, further supporting our findings that the MXene surfaces are most likely O-terminated after lithiation and the latter might be more preferred for Li intercalation.

Li Diffusion on MXenes. Facile motion of Li ions is essential for the performance of LIBs at high rates. Several different diffusion pathways for different Li coverages were examined on O-terminated MXene monolayers. The results for $Ti_3C_2O_2$, at low and high coverages, are shown in Figure S12a,b, respectively. The lowest barriers for V_2CO, Nb_2CO, Ti_2CO, and $Ti_3C_2O_2$ were 0.17, 0.24, 0.27, and 0.28 eV, respectively (Figure S12,13). These low barriers at least partially explain the large experimental rates measured[22,29,30] and compare favorably with diffusion barriers of other anode materials at low Li coverage (>0.3 eV for graphite or graphene,[44,48] 0.3−0.65 eV for TiO_2 based polymorphs).[52,53] Note that at high coverages the barrier height is closer to 0.5 eV (Figure S12b,13b)

Li Storage of f-Sc_2C and Cr_2C. In order to obtain a more thorough understanding of how Li storage capacity changes for different transition-metal carbides, we have further predicted the Li capacity of f-Sc_2C and f-Cr_2C. Although they have not been experimentally synthesized yet, simulations showed that they should be stable due to their large negative formation enthalpies.[28] Since we already know that the Li capacity of MXenes is highly dependent on the OH-free surface area, we focused on the water formation at high temperatures and H_2 formation during the first lithiation cycles of OH-terminated f-Sc_2C and f-Cr_2C. The calculated results showed that Sc_2C has high activation barriers of >1.6 and 1.18 eV (Figure S15) for reactions 2 and 3, respectively. This implies that it is more difficult to remove OH groups from f-Sc_2C surfaces and thus it will likely possess a Li capacity that is even lower than f-Ti_2C. On the other hand, f-Cr_2C has a lower energy barrier of 0.54 eV (Figure S15a) for reaction 2 and a high-energy barrier of 0.85 eV (Figure S15b) for reaction 3. The former indicates OH-free surfaces of f-Cr_2C after high-temperature annealing comparable to f-Nb_2C and f-V_2C. Therefore, the latter may have a measured capacity as high as f-V_2C.

By looking at these MXenes, we found that reaction 2 is the most important step to remove OH groups from their surfaces. Its activation barrier decreases with increased valence electron count of the transition-metal atoms. In other words, with more valence electrons, the easier it is to obtain OH-free surfaces. Among all the possible MXenes, the delaminated V_2C may possess the highest Li capacity since it has the lowest activation energies for both reactions and relatively light atoms. Furthermore, the lowest diffusion barrier of V_2C indicates good rate capability. All of these characteristics suggest the great potential of utilizing d-V_2C as anode materials for LIBs. Experimental efforts are ongoing to synthesize d-V_2C powders and optimize their surface structures.

CONCLUSIONS

We have systematically investigated the surface structures and Li-ion storage capacities of a number of functionalized MXenes using a combination of experiment and electronic structure calculations. Calculations of the Li-ion storage capacity of OH terminated MXenes do not predict sufficient capacity observed in experiment or explain the wide variations in measured capacities between different MXenes. We confirmed that after aqueous HF etching, MXenes are mostly covered by OH groups. High-temperature annealing leads to structures with fewer OH terminations. The Li-ion storage capacity is strongly dependent on the surface functional groups, with O terminated MXenes possessing the highest capacities. Calculated Li diffusion barriers also suggest high Li mobilities.

Extra Li layers can be adsorbed above already lithiated O-terminated MXenes resulting in further enhanced capacity. These additional layers are likely responsible for the measured high Li capacities of delaminated MXenes, which provide large accessible surface and available volume for the additional Li layers. The existence of a distinct mechanism for this additional capacity is supported by our XAS measurements.

Our combined experimental and theoretical findings give a description of Li-ion storage of currently synthesized MXenes useful for designing high-performance anodes for LIBs. To obtain the highest Li capacities, free-standing, O-terminated, or bare MXenes, with large surface areas, are recommended. This can be achieved with improved control over the synthesis of MXenes and proper post-processing. We also proposed a strategy to gain extra Li layers to enhance Li capacity, which explains current measured capacities and may have implications for a wide range of 2D materials.

ASSOCIATED CONTENT

Supporting Information

Snapshots of MXenes in water and at high temperatures, the lattice evolution with different OH coverage, the structure of MXenes with intercalated water layers, the vdW-DF reaction energy pathway, and the transition states of proposed reactions. This material is available free of charge via the Internet at http://pubs.acs.org.

AUTHOR INFORMATION

Corresponding Author

yxe@ornl.gov

Present Address

[#]Department of Energy and Materials Engineering, Dongguk University-Seoul, Seoul, 100-715, Republic of Korea.

Notes

The authors declare no competing financial interest.

■ ACKNOWLEDGMENTS

We thank X. F. Zhou and Kevin M. Cook for useful discussion. Boris Dyatkin and Chang E. Ren are acknowledged for their help in the vacuum annealing process and synthesis of Ti_3C_2, respectively. The neutron scattering experiment at Oak Ridge National Laboratory's Spallation Neutron Source was sponsored by the Scientific User Facilities Division, Office of Basic Energy Sciences, US Department of Energy. Computational work performed at ORNL was supported as part of the Fluid Interface Reactions, Structures and Transport (FIRST) Center, an Energy Frontier Research Center funded by the US Department of Energy, Office of Science, Office of Basic Energy Sciences. Computations used resources of the National Energy Research Scientific Computing Center, which is supported by the Office of Science of the U.S. Department of Energy under contract no. DE-AC02-05CH11231. Work done at Drexel University and Brookhaven National Laboratory (BNL) was supported by the Assistant Secretary for Energy Efficiency and Renewable Energy, Office of Vehicle Technologies of the U.S. Department of Energy under contract no. DE-AC02-05CH11231, subcontract no. 6951370 for Drexel, and contract no. DE-AC02-98CH10886 for BNL, under the Batteries for Advanced Transportation Technologies (BATT) Program.

■ REFERENCES

(1) Tarascon, J. M.; Armand, M. *Nature* **2001**, *414*, 359.
(2) Dahn, J. R.; Zheng, T.; Liu, Y.; Xue, J. S. *Science* **1995**, *270*, 590.
(3) Winter, M.; Besenhard, J. O.; Spahr, M. E.; Novak, P. *Adv. Mater.* **1998**, *10*, 725.
(4) Yang, S.; Feng, X.; Ivanovici, S.; Müllen, K. *Angew. Chem., Int. Ed.* **2010**, *49*, 8408.
(5) Poizot, P.; Laruelle, S.; Grugeon, S.; Dupont, L.; Tarascon, J. M. *Nature* **2000**, *407*, 496.
(6) Cabana, J.; Monconduit, L.; Larcher, D.; Palacín, M. R. *Adv. Mater.* **2010**, *22*, E170.
(7) Reddy, M.; Yu, T.; Sow, C.-H.; Shen, Z. X.; Lim, C. T.; Subba Rao, G.; Chowdari, B. *Adv. Funct. Mater.* **2007**, *17*, 2792.
(8) Ban, C.; Wu, Z.; Gillaspie, D. T.; Chen, L.; Yan, Y.; Blackburn, J. L.; Dillon, A. C. *Adv. Mater.* **2010**, *22*, E145.
(9) Lou, X. W.; Wang, Y.; Yuan, C.; Lee, J. Y.; Archer, L. A. *Adv. Mater.* **2006**, *18*, 2325.
(10) Idota, Y.; Kubota, T.; Matsufuji, A.; Maekawa, Y.; Miyasaka, T. *Science* **1997**, *276*, 1395.
(11) Chan, C. K.; Peng, H.; Liu, G.; McIlwrath, K.; Zhang, X. F.; Huggins, R. A.; Cui, Y. *Nat. Nanotechnol.* **2007**, *3*, 31.
(12) Chan, C. K.; Zhang, X. F.; Cui, Y. *Nano Lett.* **2007**, *8*, 307.
(13) Reddy, M.; Subba Rao, G.; Chowdari, B. *Chem. Rev.* **2013**, *113*, 5364.
(14) McDowell, M. T.; Lee, S. W.; Nix, W. D.; Cui, Y. *Adv. Mater.* **2013**, *25*, 4966.
(15) Butler, S. Z.; Hollen, S. M.; Cao, L.; Cui, Y.; Gupta, J. A.; Gutiérrez, H. R.; Heinz, T. F.; Hong, S. S.; Huang, J.; Ismach, A. F.; Johnston-Halperin, E.; Kuno, M.; Plashnitsa, V. V.; Robinson, R. D.; Ruoff, R. S.; Salahuddin, S.; Shan, J.; Shi, L.; Spencer, M. G.; Terrones, M.; Windl, W.; Goldberger, J. E. *ACS Nano* **2013**, *7*, 2898.
(16) Yoo, E.; Kim, J.; Hosono, E.; Zhou, H.-s.; Kudo, T.; Honma, I. *Nano Lett.* **2008**, *8*, 2277.
(17) Xiao, J.; Choi, D.; Cosimbescu, L.; Koech, P.; Liu, J.; Lemmon, J. P. *Chem. Mater.* **2010**, *22*, 4522.
(18) Naguib, M.; Kurtoglu, M.; Presser, V.; Lu, J.; Niu, J.; Heon, M.; Hultman, L.; Gogotsi, Y.; Barsoum, M. W. *Adv. Mater.* **2011**, *23*, 4248.
(19) Naguib, M.; Mashtalir, O.; Carle, J.; Presser, V.; Lu, J.; Hultman, L.; Gogotsi, Y.; Barsoum, M. W. *ACS Nano* **2012**, *6*, 1322.
(20) Naguib, M.; Mochalin, V. N.; Barsoum, M. W.; Gogotsi, Y. *Adv. Mater.* **2013**, *27*, 992.
(21) Barsoum, M. W. *MAX Phases: Properties of Machinable Ternary Carbides and Nitrides*; Wiley VCH GmbH & Co.: Weinheim, Germany, 2013.
(22) Mashtalir, O.; Naguib, M.; Mochalin, V. N.; Dall'Agnese, Y.; Heon, M.; Barsoum, M. W.; Gogotsi, Y. *Nat. Commun.* **2013**, *4*, 1716.
(23) Lukatskaya, M. R.; Mashtalir, O.; Ren, C. E.; Dall'Agnese, Y.; Rozier, P.; Taberna, P. L.; Naguib, M.; Simon, P.; Barsoum, M. W.; Gogotsi, Y. *Science* **2013**, *341*, 1502.
(24) Chang, F.; Li, C.; Yang, J.; Tang, H.; Xue, M. *Mater. Lett.* **2013**, *109*, 295.
(25) Naguib, M.; Halim, J.; Lu, J.; Cook, K. M.; Hultman, L.; Gogotsi, Y.; Barsoum, M. W. *J. Am. Chem. Soc.* **2013**, *135*, 15966.
(26) Enyashin, A. N.; Ivanovskii, A. L. *J. Phys. Chem. C* **2013**, *117*, 13637.
(27) Xie, Y.; Kent, P. R. C. *Phys. Rev. B* **2013**, *87*, 235441.
(28) Khazaei, M.; Arai, M.; Sasaki, T.; Chung, C. Y.; Venkataramanan, N. S.; Estili, M.; Sakka, Y.; Kawazoe, Y. *Adv. Funct. Mater.* **2013**, *23*, 2185.
(29) Naguib, M.; Come, J.; Dyatkin, B.; Presser, V.; Taberna, P.-L.; Simon, P.; Barsoum, M. W.; Gogotsi, Y. *Electrochem. Commun.* **2012**, *16*, 61.
(30) Come, J.; Naguib, M.; Rozier, P.; Barsoum, M. W.; Gogotsi, Y.; Taberna, P. L.; Morcrette, M.; Simon, P. *J. Electrochem. Soc.* **2012**, *159*, A1368.
(31) Tang, Q.; Zhou, Z.; Shen, P. *J. Am. Chem. Soc.* **2012**, *134*, 16909.
(32) Blöchl, P. E. *Phys. Rev. B* **1994**, *50*, 17953.
(33) Kresse, G.; Furthmüller, J. *Phys. Rev. B* **1996**, *54*, 11169.
(34) Perdew, J. P.; Burke, K.; Ernzerhof, M. *Phys. Rev. Lett.* **1996**, *77*, 3865.
(35) Dion, M.; Rydberg, H.; Schröder, E.; Langreth, D. C.; Lundqvist, B. I. *Phys. Rev. Lett.* **2004**, *92*, 246401.
(36) Klimeš, J.; Bowler, D. R.; Michaelides, A. *Phys. Rev. B* **2011**, *83*, 195131.
(37) Nosé, S. *J. Chem. Phys.* **1984**, *81*, 511.
(38) Henkelman, G.; Uberuaga, B. P.; Jónsson, H. *J. Chem. Phys.* **2000**, *113*, 9901.
(39) Mashtalir, O.; Naguib, M.; Dyatkin, B.; Gogotsi, Y.; Barsoum, M. W. *Mater. Chem. Phys.* **2013**, *139*, 147.
(40) Enyashin, A. N.; Ivanovskii, A. L. *J. Phys. Chem. C* **2013**, *117*, 13637.
(41) Chen, J. G. *Surf. Sci. Rep.* **1997**, *30*, 1.
(42) Borghols, W. J.; Lützenkirchen-Hecht, D.; Haake, U.; Chan, W.; Lafont, U.; Kelder, E. M.; van Eck, E. R.; Kentgens, A. P.; Mulder, F. M.; Wagemaker, M. *J. Electrochem. Soc.* **2010**, *157*, A582.
(43) Lafont, U.; Carta, D.; Mountjoy, G.; Chadwick, A. V.; Kelder, E. M. *J. Phys. Chem. C* **2009**, *114*, 1372.
(44) Fan, X.; Zheng, W. T.; Kuo, J.-L. *ACS Appl. Mater. Interfaces* **2012**, *4*, 2432.
(45) Buldum, A.; Tetiker, G. *J. Appl. Phys.* **2013**, *113*, 154312.
(46) Kittel, C. *Introduction to solid state physics*, 8th ed.; Wiley: New York, 2005.
(47) Chan, K. T.; Neaton, J. B.; Cohen, M. L. *Phys. Rev. B* **2008**, *77*, 235430.
(48) Zhou, L.-J.; Hou, Z. F.; Wu, L.-M. *J. Phys. Chem. C* **2012**, *116*, 21780.
(49) Chan, K. T.; Neaton, J.; Cohen, M. L. *Phys. Rev. B* **2008**, *77*, 235430.
(50) Garay-Tapia, A. M.; Romero, A. H.; Barone, V. *J. Chem. Theory Comput.* **2012**, *8*, 1064.
(51) Meng, Y. S.; Arroyo-de Dompablo, M. E. *Energy Environ. Sci.* **2009**, *2*, 589.

(52) Koudriachova, M. V.; Harrison, N. M.; de Leeuw, S. W. *Phys. Rev. Lett.* **2001**, *86*, 1275.
(53) Wagemaker, M.; van de Krol, R.; Kentgens, A. P. M.; van Well, A. A.; Mulder, F. M. *J. Am. Chem. Soc.* **2001**, *123*, 11454.